

## Investigation of coherent acoustic phonons in terahertz quantum cascade laser structures using femtosecond pump-probe spectroscopy

Axel Bruchhausen,<sup>1,a)</sup> James Lloyd-Hughes,<sup>2</sup> Mike Hettich,<sup>1</sup> Raphael Gebbs,<sup>1</sup> Martin Grossmann,<sup>1</sup> Oliver Ristow,<sup>1</sup> Albrecht Bartels,<sup>1</sup> Milan Fischer,<sup>3</sup> Mattias Beck,<sup>3</sup> Giacomo Scalari,<sup>3</sup> Jérôme Faist,<sup>3</sup> Alok Rudra,<sup>4</sup> Pascal Gallo,<sup>4</sup> Eli Kapon,<sup>4</sup> and Thomas Dekorsy<sup>1,b)</sup>

<sup>1</sup>*Department of Physics and Center for Applied Photonics, University of Konstanz, D-78457, Germany*

<sup>2</sup>*Department of Physics, Clarendon Laboratory, University of Oxford, Parks Road, Oxford OX1 3PU, United Kingdom*

<sup>3</sup>*Institute of Quantum Electronics, ETH Zurich, CH-8093 Zurich, Switzerland*

<sup>4</sup>*Laboratory of Physics of Nanostructures, Ecole Polytechnique Federale de Lausanne (EPFL), Switzerland*

(Received 24 January 2012; accepted 11 July 2012; published online 8 August 2012)

The dynamics of acoustic vibrations in terahertz quantum cascade laser structures (THz-QCLs) is studied by means of femtosecond pump-probe spectroscopy. The phonon modes are characterized by the folding of the acoustic dispersion into an effective reduced Brillouin zone. An accurate identification of this dispersion allows the sample structure and periodicity to be determined with high precision on the order of 0.1%. By temperature tuning the energy of the electronic levels of the system and performing wavelength dependent measurements, we are able to study the impulsive resonant generation and detection of coherent acoustic phonon modes. These results are supported by simulations of the electronic system that well explain the experimental observations. The effects of interface (IF) roughness on coherent acoustic phonon spectra are clearly observed for equal nominal THz-QCL structures but with different interface qualities. © 2012 American Institute of Physics. [<http://dx.doi.org/10.1063/1.4745044>]

The precise determination of the structural parameters and interface (IF) properties of semiconductor heterostructures is a long-standing issue and a major challenge for many applications in fundamental physics and technology. For the case of devices like interband cascade lasers,<sup>1</sup> mid infrared quantum cascade lasers (QCLs),<sup>2</sup> and terahertz QCLs (THz-QCLs),<sup>3</sup> the structural parameters determine their functionality. These devices have attracted much interest during the past decade as efficient sources of coherent electromagnetic radiation. Many aspects regarding basic physics and technology of the THz-QCL remain challenging and are the driving force of ongoing investigations.<sup>4</sup> QCLs rely upon intersubband electronic transitions arising from quantum confinement in heterostructures.<sup>2–5</sup> The accurate spacing of energy levels corresponding to THz frequencies requires nanofabrication with monolayer accuracy. Because of the small separation between the subbands, heating, electron-electron scattering, and the scattering of carriers with phonons play essential roles, limiting the operation of such devices to low temperatures.<sup>6</sup> A thorough understanding of the impact of structural quality and interface disorder on device performance, as well as the characterization of the existing vibrational states, i.e., their frequencies, lifetime, and their interaction with carriers, is hence crucial.

In this work, we present the first investigation of the full acoustic vibrational dynamics in THz-QCLs by femtosecond spectroscopy. We perform a thorough characterization of the

phonon acoustic states, and obtain information on the lifetime of the vibrations, show the importance of considering the proper dispersion to describe these modes, and analyse the influence of the interface roughness on the generated phonon spectrum. From the frequencies of the generated coherent acoustic phonons, we accurately establish the structural parameters of the QCL's active region. By temperature tuning the electronic eigenstates of the QCL structure, we analyse the photon–electron–phonon coupling in detail.

We have analysed a series of III-V based THz-QCL structures. In this work, we will discuss two particular sets of THz-QCL structures, which have been extensively studied and characterized from the point of view of their device performance and lasing efficiency.<sup>7,8</sup> The structure of a typical QCL sample consists of an optically active region comprising a superlattice (SL) formed by a complex period of doped and intrinsic semiconductor layers.

The first THz-QCL sample, based on a three quantum well (QW) active module and designed to emit at about 3 THz,<sup>7</sup> was grown by molecular beam epitaxy (MBE) on a (001) GaAs substrate paying special attention to the interface quality. The nominal layer structure of one SL period is [Al<sub>0.03</sub>Ga<sub>0.97</sub>As (32.5 nm)/Al<sub>0.15</sub>Ga<sub>0.85</sub>As (3.2 nm)/GaAs (16.6 nm)/Si: Al<sub>0.15</sub>Ga<sub>0.85</sub>As (4.3 nm)/Si: GaAs (10.0 nm)/Al<sub>0.15</sub>Ga<sub>0.85</sub>As (3.7 nm)]. This period is repeated 180 times. The Si doping of the 4th and 5th layers is  $N_d \sim 2.05 \times 10^{16} \text{ cm}^{-3}$  and  $N_d \sim 2.4 \times 10^{16} \text{ cm}^{-3}$ , respectively.

The second set of samples consists of two THz-QCL structures based on the bound-to-continuum principle with a single-quantum-well phonon extraction/injection stage, also designed to emit around 3 THz.<sup>8</sup> Both structures were grown

<sup>a)</sup>Also at IB & CAB (CNEA) and CONICET, Bariloche, Argentina. E-mail: Axel.Bruchhausen@uni-konstanz.de.

<sup>b)</sup>E-mail: Thomas.Dekorsy@uni-konstanz.de.

by low-pressure organo-metallic chemical vapor deposition (OMCVD)<sup>9</sup> with the *same* nominal SL period defined as [GaAs (11.0 nm)/Al<sub>0.15</sub>Ga<sub>0.85</sub>As (1.8 nm)/GaAs (11.5 nm)/Al<sub>0.15</sub>Ga<sub>0.85</sub>As (3.5 nm)/GaAs (9.4 nm)/Al<sub>0.15</sub>Ga<sub>0.85</sub>As (3.9 nm)/Si:GaAs (18.4 nm)/Al<sub>0.15</sub>Ga<sub>0.85</sub>As (4.8 nm)]. The total number of period is 158 times. Here the Si doping of the 4th layer is  $N_d \sim 2.0 \times 10^{16} \text{ cm}^{-3}$ . More specific details about these samples will be given later.

The samples were investigated using high-speed asynchronous optical sampling (ASOPS).<sup>10–12</sup> This pump-probe technique is based on two asynchronously linked femtosecond Ti:sapphire ring lasers of repetition rate  $f_R \sim 1 \text{ GHz}$ ,<sup>10</sup> where one laser provides the pump pulses and the second laser the probe pulses. The time delay between both pulse trains is realized through an actively stabilized 5 kHz repetition-rate-offset  $\Delta f_R$  between the two lasers, which allows the stroboscopic stretching of the time between two consecutive excitation pulses with a linear increment in time delay of 5 fs. The temporal modulation of the probe-beam's reflectivity ( $\Delta R/R$ ) on the sample is recorded with a detector of  $\sim 120 \text{ MHz}$  bandwidth, resulting in a time resolution of less than 60 fs and a signal-to-noise ratio above  $10^7$ . Further details on the ASOPS technique are discussed elsewhere.<sup>11,12</sup> Both laser beams, with central wavelength of 790 nm for the pump and 810 nm for the probe beams and typical average power of  $\sim 100 \text{ mW}$  and  $\sim 10 \text{ mW}$ , respectively, are focused on the sample to a  $50 \mu\text{m}$  diameter spot.

The transient reflectivity changes  $\Delta R/R$  are characterized by a sharp onset at time delay  $t=0 \text{ ps}$ , followed by a multiple-exponential decay, corresponding to the reflectivity modulation due to interband carrier excitation.<sup>13</sup> This electronic contribution is subtracted in order to obtain the oscillating signal due to coherently generated acoustic phonons. An example of these extracted oscillations obtained at room temperature for the first sample is shown in Fig. 1(a). These oscillations result from a combination of long lived high frequency modes (up to  $\sim 1 \text{ THz}$ ) that contain rich information, and can be well observed until the end of the window of observation. This demonstrates that these coherent generated phonons remain and persist within the structure at least until this window's end, i.e.,  $\sim 1 \text{ ns}$ . Hence these acoustic modes present a potential problem for the dissipation of heat within a QCL operating under continuous bias, and contributing to the dephasing of the electronic states involved in the lasing process. To analyse the spectral components of this transient signal, we show in Fig. 1(c) its numerical Fourier transform. A series of sharp peaks is observed, where the widths of most peaks is limited by the experimental resolution of  $\sim 1 \text{ GHz}$  given by the time window.

The core of a THz-QCL is given by a SL structure. Its acoustic phonon system is determined by the superperiodicity, and is characterized by the folding of the acoustic branches into a new effective reduced Brillouin zone (BZ).<sup>14,15</sup> A good description of the folded acoustic (FA) phonons is obtained using an extension of the Rytov model<sup>14,15</sup> for infinite periodic SLs containing multiple layers per period. The calculated FA phonon dispersion for the sample using this model is depicted in Fig. 1(b). The

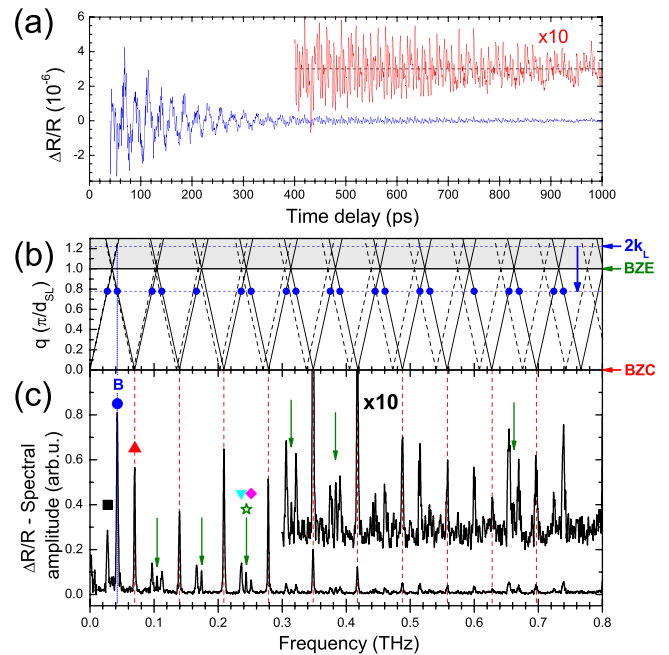


FIG. 1. (a) Extracted oscillations of a typical transient. For time delays  $t > 400 \text{ ps}$ , the transient is also shown magnified ( $\times 10$ ) and shifted vertically. (b) Calculated folded acoustic phonon dispersion according to an extended Rytov model. The dashed and full lines correspond to the nominal and thickness-corrected (by  $-3.1\%$ ) calculated dispersions, respectively. The blue dots indicate the experimentally observed  $2k_L$ -modes, which are folded into the first effective Brillouin zone as indicated by the vertical (blue) arrow. BZE (BZE) indicates the Brillouin zone center (edge) of the first effective Brillouin zone. (c) Fourier transform of the extracted oscillations shown in (a). The higher frequency part ( $> 0.3 \text{ THz}$ ) is shown magnified ( $\times 10$ ) and vertically shifted. The vertical dotted (red) lines indicate the frequency of the observed  $q=0$  modes. The peak labelled as “B” and marked by the vertical dotted (blue) line corresponds to the “bulk-like” mode, and the symbols and arrows identify the frequency of some selected peaks, which are used later in Fig. 4(d) and explained in the text.

dashed lines in this panel show the dispersion for the layer thicknesses intended in the growth process.

In pump-probe experiments, the modes that have the correct symmetry to couple to the pump and probe light consist of a combination of modes corresponding to the BZ center (BZC) with  $q=0$ , and those with effective wavevectors of  $q = 2k_L$ , where  $k_L$  is the wavevector of the probe laser light within the sample.<sup>13,16,17</sup> Consequently, the active modes form a triplet within the spectral domain. In Fig. 1(c), the equidistant BZC peaks are indicated by a vertical dashed (red) lines.

Since the composition of each layer is well known, it is possible to adjust the calculated FA phonon branches to the measured BZC frequencies by varying the individual layer's thicknesses  $d_i$  of the SL and using the well established bulk parameters for AlGaAs-compounds.<sup>18</sup> The best agreement is obtained for a uniform reduction of the nominal layer thickness  $d_i$  by  $3.1\%$ . The resulting dispersion is shown with full lines in Fig. 1(b). This reduction is in agreement with x-ray diffraction (XRD) measurements performed on this sample. Thanks to the observation of the large number of branches (up to the 22nd order, one of the highest orders observed in zone-folded systems), and to the higher structural sensitivity provided by the higher modes, we can establish a very

accurate estimation of the real structure with a 0.1% accuracy, limited mainly by the peak's experimental line width given by the repetition rate  $f_R \sim 1$  GHz. Such precision is obtainable with conventional XRD-systems in characteristic times of several hours, and with a lateral resolution of a few mm. This is in strong contrast to the results presented here, which only required a few minutes of data acquisition. The lateral resolution in the pump-probe experiment is given by the optical spot size, and enables very fast scans over the sample,<sup>12</sup> which is of particular interest, e.g., to establish the uniformity along the whole sample.

The accuracy of the structural determination is further demonstrated when the position of the measured  $2k_L$ -modes is compared to the predicted ones. As indicated by the horizontal dashed (blue) line in Fig. 1(b), the value of  $2k_L$  for this sample exceeds by 22% the first BZ, determined by the BZ edge (BZE) wavevector ( $q = \pi/d_{SL} < 2k_L$ ), and falls into the second reduced BZ [shaded area in Fig. 1(b)]. As a consequence, the effective  $q = 2k_L$  wavevector is additionally folded into the first BZ as indicated by the arrow and the additional horizontal dotted (blue) line. The intersection between this additional line and the calculated dispersion indicate the position of the active  $2k_L$ -modes. Note that due to the additional folding of the  $2k_L$ -modes, it is possible to observe an additional peak to the lower frequency side of the "bulk-like" mode [indicated as "B" in Fig. 1(c)].<sup>19</sup> The (blue) dots in this plot indicate the corresponding position of the experimentally observed peaks. The frequency matching is remarkable. This good agreement together with the observation of 22 FA branches is a strong indication of an excellent periodicity and interface quality in the sample. A further spectral feature is the systematic appearance of peaks that precisely match the BZE mode frequencies. These peaks are identified in Fig. 1(c) by the vertical arrows. The fact that these edge-peaks are observed experimentally, though symmetry forbidden, will be addressed later.

The dynamical aspects of the acoustic vibrations, together with the analysis of the lifetime of the coherent generated oscillations in this sample, are better evidenced in Fig. 2. On the right panel, we present a contour-plot of a short-time numerical Fourier transform for the transient reflectivity changes of the sample at room temperature. It was accomplished by using a gliding Welch-type window that accounts for 200 ps.<sup>20</sup> This temporal width is a good compromise to have a reasonable frequency resolution  $\sim 5$  GHz and to observe the evolution with time of the different frequency components. The panel on the left in Fig. 2 compares the numerical Fourier transform of the same reflectivity oscillations accounting the entire window of observation in order to identify each of the modes. As expected, the more general evolution displays peaks that have amplitudes with a decreasing behaviour in time. However, as can be observed, the amplitude decay and evolution differs very strongly depending on each mode. The behaviour can basically be divided in two groups, and is strongly determined by the nature of the mode. On the one hand, we can discriminate exponentially like decaying modes. These later basically embrace the active  $2k_L$ -modes [see Fig. 1(b)]. These modes, although extended throughout the entire sample,

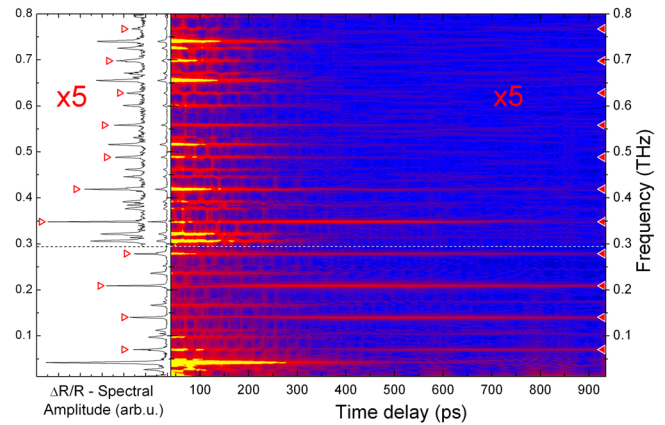


FIG. 2. Short-time numerical Fourier transform of a transient equivalent to the one shown in Fig. 1(b). For the graph shown here, the gliding Welch-window has been set to 200 ps. The panel on the left shows the numerical Fourier transform accounting the entire window of observation. The regions for frequencies above 0.3 THz are displayed magnified ( $\times 5$ ) as indicated and shifted. The triangles indicate the frequency of the long lived BZC modes with effective wavevector  $q = 0$ .

have an effective non-zero propagating component, which causes the acoustic vibrations to leave the region of observation given by the penetration depth of the probe light. Most of these components can be described in time by a multiple-exponential decay, and vanish in times that comprise  $\sim 300$  ps up to  $\sim 700$  ps. On the other hand, the modes generated near the BZC have an effective wave-vector of  $q \simeq 0$  and with nearly zero group velocity,<sup>14</sup> i.e., they represent modes that are quasi-non-propagating or standing-wave like. Their presence within the time window of observation clearly exceeds the 1 ns of our window of observation. This behaviour is undoubtedly observed up to the end of the time-window for the first six BZC modes. The frequencies of the BZC modes are indicated in Fig. 2 by the equispaced triangles, and clearly correspond to the horizontal parallel brighter regions. For higher frequencies, the overall intensities are weaker and it is not possible to distinguish their presence from the noise level for larger times ( $\geq 500$  ps). BZ edge modes with an effective wavevector of  $q = \pi/d_{SL}$ , also have a near-zero group velocity and are thus also quasi-non-propagating. In a similar way to the BZC modes, the two lower BZE modes at  $\sim 0.1$  THz and  $\sim 0.17$  THz, respectively, are also weakly but clearly observable at the end of the temporal window (see Fig. 2, right panel) showing lifetimes that exceed 1 ns.

We performed temperature dependent pump-probe measurements in order to further investigate coherent phonon generation, and to analyse the vibrational states at the typical operating temperatures of THz-QCLs. For these measurements, we used degenerate pump and probe wavelengths, centred at  $\lambda_0 = 825$  nm ( $h\nu_0 = 1.503$  eV) and with a spectral width (FWHM) of about  $\Delta\lambda \simeq 20$  nm ( $h\Delta\nu_0 = 40$  meV). A typical spectrum of the probe laser wavelength is shown in Fig. 4(c). The measured  $\Delta R/R$  transients for temperatures varying from 300 K down to 4.5 K are shown in Fig. 3(a). From room temperature down to about 150 K, a strong positive electronic signal can be identified at  $t=0$  ps. Between 150 K and 100 K, the electronic component flips from positive to negative. Figure 3(b) shows the FA phonon oscillations

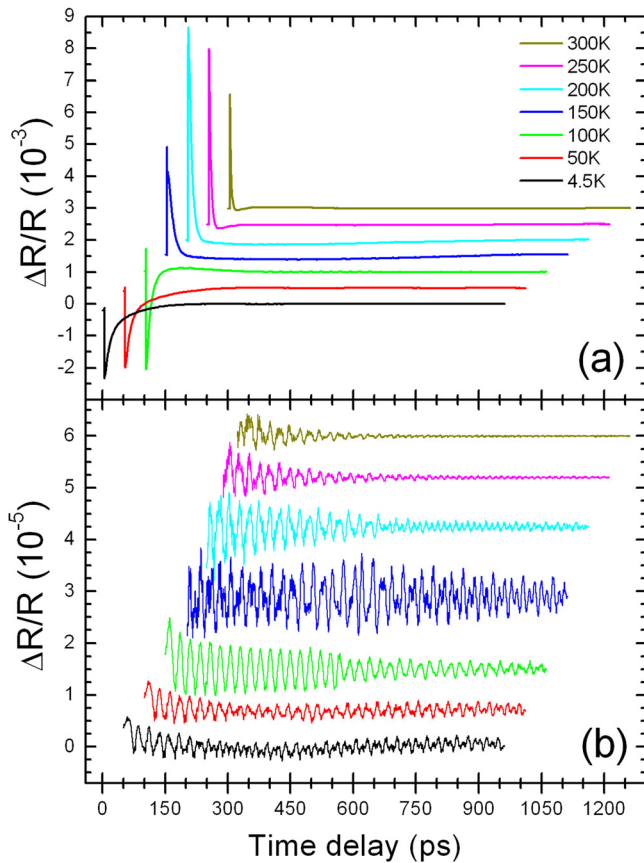


FIG. 3. Time resolved reflectivity changes  $\Delta R/R$  for different lattice temperatures. (b) Extracted coherent acoustic phonons dynamics of the data in (a). The transients are shown horizontally (each by 50 ps) and vertically shifted for clarity.

extracted from the transients in Fig. 3(a). From 300 K to 200 K, the amplitude of the oscillations grows, and their lifetime increases slightly. At 150 K, a dramatic change in the transient is observed, where the shape of the oscillations becomes different. Below 100 K, the transients look very similar, and again no evident differences can be distinguished. Clearly, the lifetime of the coherent oscillations approaches or exceeds 1 ns.

This behaviour demonstrates an important relation between the electronic states of the THz-QCL, their evolution with temperature, and their coupling to the coherent phonons and the photoexcitation. In order to analyse this temperature difference and to interpret it in a more quantitative way, we calculated the heterostructure's electron and hole bandstructure by solving the Schrödinger-Poisson equation at each temperature.<sup>21</sup> An example of such a calculated bandstructure is shown in Fig. 4(a) for  $T = 150$  K. The figure shows the conduction band (CB) and valence band (VB) profiles (black lines), together with the different electron and hole squared eigenfunctions within one SL period. The electronic states, although slightly de-localized through the entire SL period, can be well assigned to each of the constituting QWs. The E1H1 direct transition for the middle well has the lowest energy, with an energy of  $\sim 1.5$  eV at 150 K.

The energy of the direct optical (dipole-allowed) interband transitions as function of temperature are depicted in

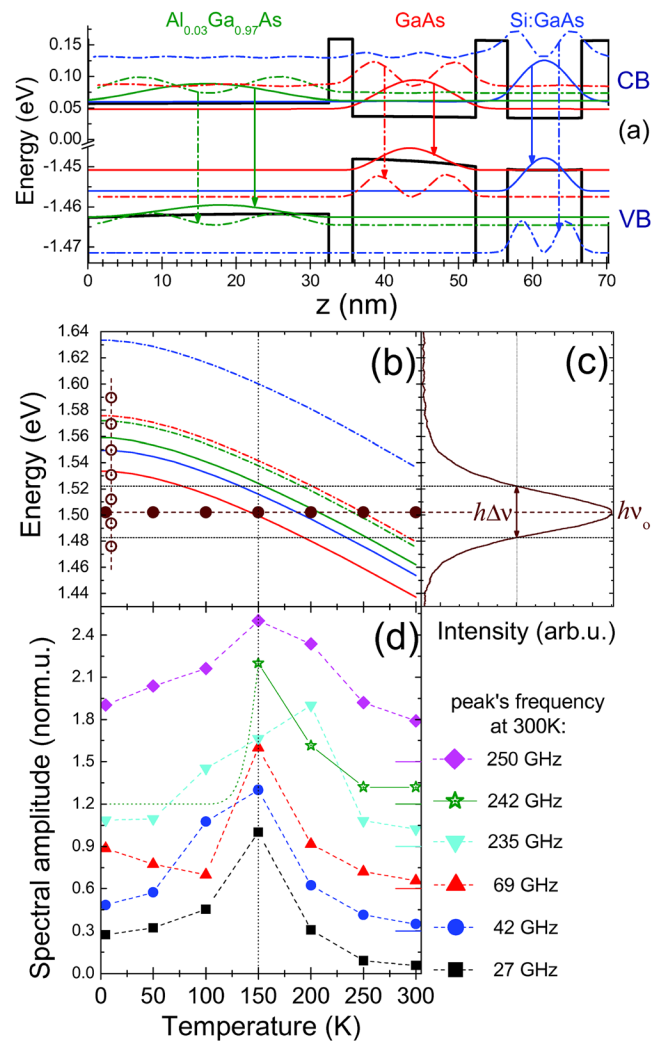


FIG. 4. (a) Bandstructure profile along the growth axis ( $z$ ) for one superlattice period (left axis). The squared electron and hole wave function, calculated for  $T = 150$  K are shown superimposed. The E1H1 direct transition for the middle well has the lowest transition energy (solid red arrow). (b) Calculated dipole-allowed interband transition energies as a function of temperature. The curve style and colour match the vertical arrows of panel (a) that indicate the corresponding transition. The full (empty) dots indicate the experimental points for temperature (probe wavelength) dependent measurements. (c) Typical spectrum of the laser, where the horizontal dashed line indicates the central energy ( $h\nu_0$ ), and  $h\Delta\nu$  delimits the FWHM of the spectrum. (d) Normalized (to the maximum) spectral amplitude as function of temperature of the modes indicated in Fig. 1(c) using the same symbols. The curves are shifted vertically (each by 0.3), and the lines are guides to the eye.

Fig. 4(b), where the E1H1 and E2H2 transitions are plotted as full and dashed-dotted lines, respectively. The curves (red, blue, and green) correspond, respectively, to transitions at the middle, right, and left QWs of the bandstructure, as schematized in Fig. 4(a) by the style-matching vertical arrows. As the temperature is reduced, the transition energies increase in accordance to the Varshni equation.<sup>22</sup> Following the horizontal dashed line indicating  $h\nu_0$ , starting from high temperatures, it is noticeable that the excitation and detection energies clearly lie above the main electronic transition energies. At a temperature of about 150 K, the central energy of the laser coincides with the lowest possible optical transition energy. The excitation regime therefore changes gradually, moving from a situation where real carriers are excited,

passing through a transition region ( $75\text{ K} < T < 175\text{ K}$ ) where only the lowest QW states are resonantly excited, to finally a situation where the excitation of the carriers happens well below the main electronic states ( $T < 75\text{ K}$ ). This gradual transition from real to virtual excitation has strong consequences regarding the selectivity of the optically generated coherent phonons.<sup>13,23–25</sup> This conceptually explains the abrupt sign change of the electronic contribution to  $\Delta R/R$  observed between 150 K and 100 K [see Fig. 3(a)], and the change in the acoustic components in Fig. 3(b). Note in Fig. 4(b) that for the three highest temperatures the entire spectral range  $\Delta\nu$  falls above the lowest E1H1 energy. Here, for  $T > 175\text{ K}$ , due to the spectral extension of the laser pulse the differences in the oscillation transients are mainly explained by the slight changes in the dielectric function close to resonances, the changes in the absorption length, and the differences in the QW's electronic states that are excited and probed.<sup>13</sup> The main changes happen for  $75\text{ K} < T < 175\text{ K}$ , i.e., the transition region, where the overlap of  $\Delta\nu$  with the lower QW-states changes fundamentally. Finally, at the two lowest temperatures ( $T < 75\text{ K}$ , where  $\Delta\nu$  lies completely below the lowest E1H1) no substantial changes in the acoustic phonon transients are witnessed [Fig. 3(b)].

The normalized spectral amplitude of some selected peaks is illustrated in Fig. 4(d). These peaks are identified by the corresponding symbol type in Fig. 1(c). As expected, when decreasing the temperature the peaks shift slightly (1% to 2%) to higher frequencies due to the thermal expansion coefficient. Note that the normalized amplitude dependence [see Fig. 4(d)] for temperatures above 150 K is similar for many of the peaks, in agreement with the similar oscillation shape observed in the extracted transient in Fig. 3(b).

The complete theoretical modelling of the opto-acoustic coupling including the quantum confined states should allow the calculation of the observed time-dependent modes' spectra in frequency, amplitude, and temperature. However, for the moment too many parameters, especially the photoelastic constants of the involved doped and intrinsic ternary alloys, are not accurately known hindering the quantitative description of the individual spectral amplitude of the acoustic modes. Nevertheless, the general behaviour of the Fourier amplitude is similar for most of the peaks, showing a clear maximum around 150 K and decreasing for temperatures above and below.

The BZE modes, clearly present at room temperature [see peaks marked by vertical arrow in Fig. 1(c)], are completely absent at low temperatures, and appear abruptly when increasing  $T \geq 150\text{ K}$ . This appearance is attributed to a symmetry breakdown related to the resonance effects together with the effects of the doping of some of the constituting layers, which make these modes active.<sup>25</sup> As an example, the spectral amplitude of one of the BZE-modes, the one at 242 GHz, is shown additionally in Fig. 4(d) (empty stars).

We observe a similar resonant behaviour of the generated coherent acoustic modes varying the central wavelength of the probe laser pulse ( $\lambda_{\text{probe}}$ ) from 840 to 780 nm (i.e., 1.49 to 1.59 eV, respectively), for a fixed central pump laser

wavelength of 780 nm (1.59 eV), and a constant temperature of 10 K. These results are summarized in Fig. 5. Figure 5(a) shows the obtained transients. The situation for each of these transients with respect to the direct dipole-allowed interband QW transitions of the structure is indicated on the energy vs. temperature landscape in Fig. 4(b) by the empty circles and the vertical dashed line. Following the transients in Fig. 5(a) from higher to lower probe energies, i.e., for increasing  $\lambda_{\text{probe}}$ , the onset of the signal suffers a sudden flip from positive to negative when probing above and below the lowest electronic interband transition (E1H1) [see Fig. 4(b)], i.e., when the detection mechanism occurs due to the coupling to real carriers in the absorbing range to a regime where the sample is more transparent and the coupling is more virtual.<sup>13,23–25</sup> In fact, the curve corresponding to  $\lambda_{\text{probe}} = 810\text{ nm}$  (middle curve) shows an intermediate situation, where an initial very fast negative onset coexists with the positive multiple-exponential decay observed for lower probe wavelengths. Here the probe's central wavelength, as

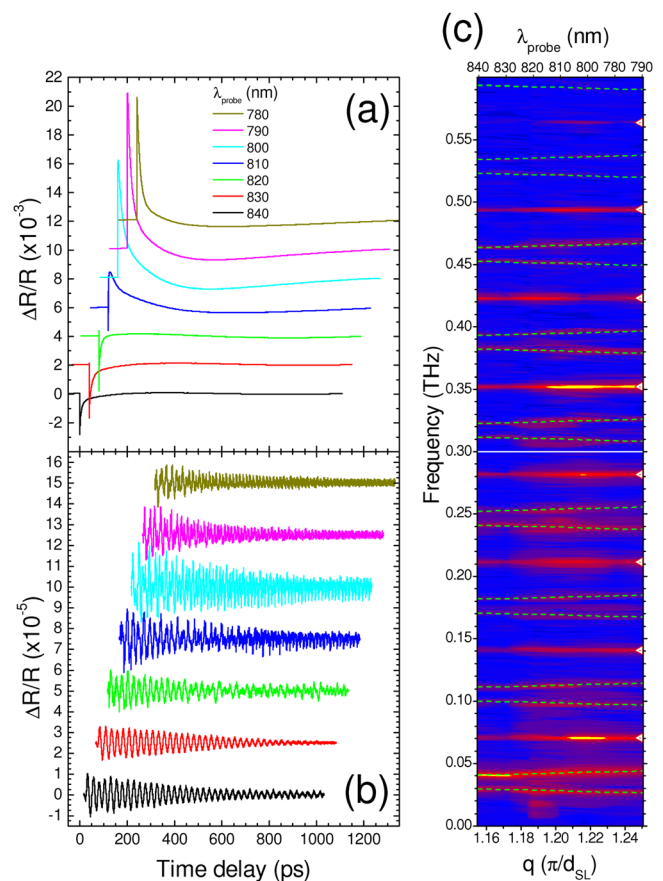


FIG. 5. Time resolved reflectivity changes  $\Delta R/R$  at  $T = 10\text{ K}$ , for a fixed pump laser wavelength of  $\lambda_{\text{pump}} = 780\text{ nm}$  (1.59 eV) and varying probe laser wavelength  $\lambda_{\text{probe}}$  (as indicated). (b) Extracted coherent acoustic phonon dynamics of the data shown in (a). The transients in (a) and (b) are shown horizontally (each by 50 ps) and vertically shifted for clarity. (c) Contour plot depicting the spectral amplitude of the numerical Fourier transformation of the extracted phonon oscillations as function of the frequency of the modes (y-axis) and the effective normalized phonon wavevector  $q$  (x-axis). The top x-axis indicates the corresponding probe wavelength. The dashed (green) lines indicate the calculated folded acoustic phonon dispersion within the second Brillouin zone. The contour plot has been smoothed and the logarithmic scale fixed for frequencies  $> 0.3\text{ THz}$  to better observe the mode evolution.

observed in Fig. 4(b), matches the lowest interband transition (E1H1) at 10 K almost resonantly. In all experiments, the probe's spectral profile and width for varying central wavelengths remains equivalent to the one shown in Fig. 4(c). Note how Fig. 5(a) resembles the circumstances described in Fig. 3(a) for decreasing temperature. The important difference here is that the electronic states involved in the coherent generation and detection processes are the same for each measured situation, in a sense that they are exempt of possible differences due to thermal broadening or further effects related to the temperature variation.

Figure 5(b) shows the contribution to the transient reflectivity changes  $\Delta R/R$  only due to the coherent acoustic phonon modes. A similar resemblance is found to the observations described for the temperature dependent measurements [see Fig. 3(b)]. However, one important difference is that the overall lifetimes of the oscillations are much longer, with significantly larger oscillation amplitudes at the end of the observation interval ( $\sim 1$  ns). A qualitative change in the general oscillation shape in Fig. 5(b) can be observed when  $\lambda_{\text{probe}}$  is larger than 810 nm. As can be seen from Fig. 4(b), this change coincides with the situation where the spectral FWHM of the probe laser begins to lie below the lowest electronic interband transition (E1H1), and the detection starts to become non-resonant. A similar treatment as the one shown in Fig. 2, i.e., performing a short-time windowed numerical Fourier transform for each transient, reveals that the general behaviour is maintained, and that those frequency components that are generated and detected<sup>17</sup> have a much longer extension in time. Specially the modes with  $q=0$ , besides some oscillatory behaviour—also observed at higher temperatures—are nearly undamped at the end of the observed time window. In a similar way, the observed modes corresponding to  $q = 2k_L$  display a larger general lifetime, but as expected, display a strong dependence with the penetration depth of the particular  $\lambda_{\text{probe}}$ . For instance, for shorter probe wavelength (above the E1H1 energy) since the penetration depth is less due to absorption, the observed  $2k_L$ -modes display a more damped behaviour (shorter damping time) but are still observed at the end of the observed window. Whereas if the wavelength is increased (below the E1H1 energy) the damping time increases beyond 1 ns.<sup>26</sup>

To analyse the behaviour of the different modes as function of  $\lambda_{\text{probe}}$ , we present a contour plot in Fig. 5(c) showing the spectral amplitude of the numerical Fourier transforms of the transients corresponding to the extracted phonon oscillations, some of them plotted in Fig. 5(b). The y-axis indicates the frequency of the appearing modes, the bottom x-axis indicates the effective normalized phonon wavevector in the first part of the second Brillouin zone, which coincides with  $q = 2k_L$  [see Fig. 1(b) for guidance], and the top x-axis indicates the wavelength of the probe laser  $\lambda_{\text{probe}}$  corresponding to the effective wavevector  $k_L$ . The spectra have been smoothed and rescaled for frequencies above 0.3 THz in order to better observe the evolution of the modes.

Again, the two kind of modes contribute to the spectrum. On the one hand, the equidistant *dispersionless*  $q=0$  (BZC) modes, indicated by the triangles on the right axis of Fig. 5(c). On the other hand, the  $2k_L$ -modes that display a clear wavelength dependence, following the corresponding

acoustic folded dispersion. The latter is shown superimposed to the contour plot with dashed (green) lines, calculated as described for Fig. 1(b), and accounting for the corresponding slight blue-shift of modes at low temperature ( $\sim 2\%$ ). The effective index of refraction used for calculating the effective  $k_L$  was taken as  $n_{\text{eff}} = 3.6$ , and is in reasonable agreement with the effective index estimated from published data. The real part of the index of refraction for these III-V materials varies relatively little in the optical range analysed, and justifies the selected constant value for the effective index of refraction to calculate  $k_L = \frac{2\pi}{\lambda} n_{\text{eff}}$ . As observed in Fig. 5(c), the overall agreement between the calculated dispersion and the measured peak's position is very good, describing the increasing distance between the different  $2k_L$ -pairs.

In relation to the spectral behaviour, it should be noted in Fig. 5(c) that when probing with energies well below E1H1 ( $\lambda_{\text{probe}} \leq 830$  nm), that the  $2k_L$ -modes are only weakly observed, whereas the BZC modes are predominant. A clear exception to this is the “bulk-like” peak at  $\sim 40$  GHz, which is very intense, and leading to a temporal transient where this frequency overshadows [see the two lower transient in Fig. 5(b)]. When increasing the energy between 820 and 810 nm the overall intensity of the  $2k_L$ -modes and the BZC modes become suddenly significantly enhanced, when the probe laser becomes resonant with the electronic states of the QW-system, inducing consequently more complex oscillations in time domain. In addition, for  $\lambda_{\text{probe}} \geq 830$  nm, very weakly, it is possible to observe in Fig. 5(c) the appearance of some BZE modes between the  $2k_L$ -modes, e.g., at  $\sim 105$  GHz and  $\sim 175$  GHz. The horizontal fringes that modulate the plot at low intensities are interferences that arise from the chosen color scale, which are an artefact induced by the used apodization window.

With the purpose of achieving a better understanding of the effect of the IF quality on the THz-QCLs in relation to its acoustic phonon states and dynamics, we compared a set of two samples. Both samples were grown simultaneously in the *same* run by OMCVD with exactly the same nominal structure, but on two (001) GaAs substrates which were slightly misoriented (about  $2^\circ$ ) towards different crystallographic directions, i.e., towards (111)*b* and (111)*a*, respectively.<sup>27</sup> This slight misorientation of the substrate leads to significantly different IF roughnesses, which were characterized by a root-mean-square amplitude of 280 pm over about 50 nm and 1 nm over 500 nm, respectively, for the (111)*b* and (111)*a* direction, as determined from atomic force microscopy.<sup>8</sup> For both samples, the coherent phonon spectra have been analysed at room temperature, and the spectral amplitude of the coherently generated FA phonons is shown in Fig. 6, acquired for same experimental conditions. Similar peak structures as those shown for the former sample can be identified. The top panel of this figure shows the FA phonon dispersion for comparison's sake. The dashed (red) and the dashed-dotted (green) vertical lines indicate the frequency of the BCZ modes and that of the BZE modes, respectively. Again, since  $2k_L$  is larger than the first reduced BZ ( $\sim 10\%$ ), the modes are folded back into the first reduced BZ, and the filled (blue) circles indicate the position of the modes that are observed experimentally. To have a better visibility of

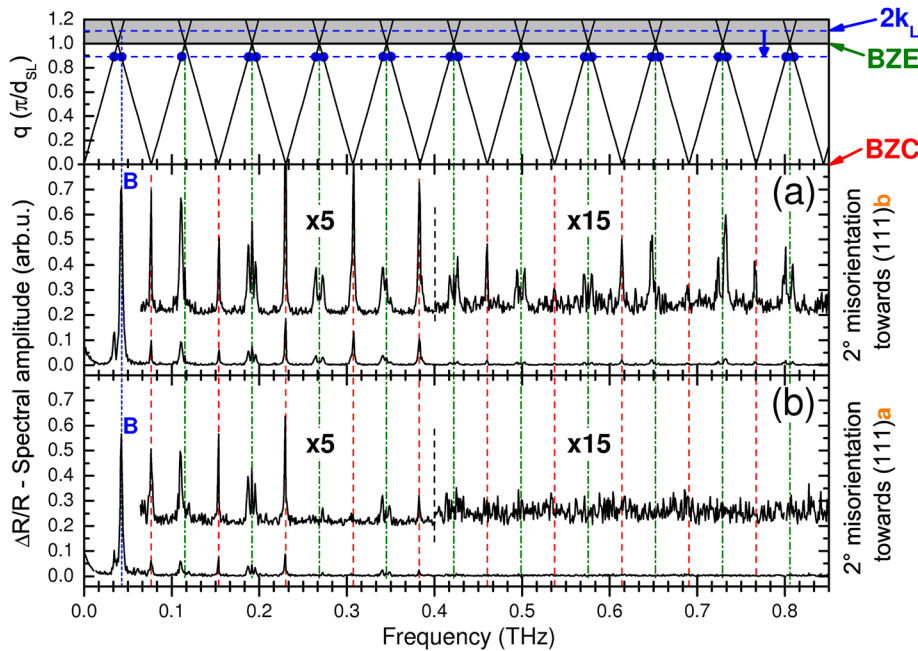


FIG. 6. (Top) Calculated folded acoustic phonon dispersion. Numerical Fourier transform of the transients obtained for the samples grown by OMCVD with different IF roughnesses accomplished by using misoriented (001) GaAs substrates: (a) misorientation towards the (111)*b* direction with less IF roughness, and (b) misorientation towards the (111)*a* direction with higher IF roughness.

the appearing modes, the spectra are shown magnified and vertically shifted: for the frequency region between  $\sim 0.07$  THz and 0.4 THz by a factor 5, and for frequencies larger than 0.4 THz by a factor of 15. Three points are important to highlight: (i) The overall good agreement of the mode's frequency. From a comparison between Figs. 6(a) and 6(b), it is immediate to see that all observed peaks' frequencies are practically the same for both samples, and coincide with the position of the BZC and BZE of the calculated dispersion curves (top). This indicates that both samples have indeed—as designed—the *same* layer structure and period. (ii) The observed peaks and their individual shapes in both samples are basically the same. (iii) The peak's spectral intensities for sample misoriented towards (111)*a* [Fig. 6(b)], are overall significantly lower, and decrease significantly faster for the higher observed modes. Whereas in Fig. 6(a) it is possible to clearly distinguish the BZC ( $q=0$ ) and  $2k_L$ -modes up to the end of the displayed range, in Fig. 6(b) for the second sample it is impossible to distinguish any clear spectral feature from the noise for the second magnified region ( $>0.4$  THz). The reason for this is attributed to the increased IF roughnesses. In a simple picture, the roughness at the interfaces between two layers can be described as a “rounding” of the materials composition and consequently of its properties with respect to the perfect atomically flat boundary between materials. Due to the periodicity of the SL, the coherent generation and optical detection processes in a pump-probe experiment can be essentially expanded in a Fourier series that involve the folded acoustic modes.<sup>28–30</sup> Consequently, in order to describe sharp interfaces, a large number of modes are needed. On the contrary, when the roughness is larger and the interfaces are smoothed, less modes are involved in the process. It is important to remark that a clear correlation has been demonstrated between the decreasing microscopic interface roughness and the improvement of the general performance, the operating temperatures, and the wider dynamical working range of the THz-QCL

devices.<sup>8</sup> The analysis of the observed generated acoustic phonons will enable an estimation of the average degree of interface roughness and quality from period to period of the SL. It is also important to clarify that the absence of higher modes in the obtained pump-probe spectrum for sample with an increased roughness [Fig. 6(b)], does not mean that the actual acoustic phonons are not present. On the contrary, the increase of roughness implies a faster loss of coherence of the involved modes by phonon scattering at the imperfect or disordered interfaces into other incoherent phonon acoustic states, with eventual further implications on the heating of the device and thus affect its performance.

In conclusion, we have characterized the dynamics of acoustic vibrations in THz quantum cascade laser structures by means of femtosecond pump-probe spectroscopy. The coherent generated phonon modes were identified with the folding of the acoustic branches due to the periodicity of the THz-QCL's active region. We have analysed the lifetime of the involved modes and have established that depending on the acoustic mode's type their presence in the active region of the device can well exceed 1 ns. We have shown that the analysis of the pump-probe active modes enables a precise estimation of the structural parameters, and can be used to characterize the average degree of interface roughness within one period of the superlattice constituting the device. By performing temperature and laser wavelength dependent measurements, we have analysed the behaviour of the coherent generated folded acoustic phonon oscillations for different electronic coupling regimes, and evidenced the important interaction of these modes with the carriers. So far, the intersubband acoustic phonon-electron scattering rates have been calculated assuming bulk-like phonons.<sup>31</sup> Nevertheless, as we have shown, the acoustic dispersion differs importantly from the bulk, and the scattering into these low-energy FA phonon modes *should* be considered when designing the active region of THz-QCLs and for a more accurate calculation of these intra- and inter-subband scattering rates. In addition, the presence of these modes and their

possible additional control by engineering and design<sup>32,33</sup> may help in bound-to-continuum designs<sup>5</sup> of THz-QCLs by contributing to the transition rate between wells in the miniband to depopulate the lower state, and possibly help to promote a more efficient heat dissipation.

A. Bruchhausen acknowledges the Alexander von Humboldt Foundation (Bonn, Germany) for financial support. This work is supported by the Deutsche Forschungsgemeinschaft (DFG) through the SFB 767, and by the Ministry of Science, Research and Arts of Baden-Württemberg (Germany).

- <sup>1</sup>C. H. Lin, R. Q. Yang, D. Zhang, S. J. Murry, S. S. Pei, A. A. Allerman, and S. R. Kutz, *Electron. Lett.* **33**, 598 (1997).  
<sup>2</sup>J. Faist, F. Capasso, D. L. Sivco, C. Sirtori, A. L. Hutchinson, and A. Y. Cho, *Science* **264**, 5158 (1994).  
<sup>3</sup>R. Köhler, A. Tredicucci, F. Beltram, H. E. Beere, E. H. Linfield, A. G. Davies, D. A. Ritchie, R. C. Iotti, and F. Rossi, *Nature* **417**, 156 (2002).  
<sup>4</sup>B. S. Williams, *Nat. Photonics* **1**, 517 (2007).  
<sup>5</sup>G. Scalari, L. Ajili, J. Faist, H. Beere, E. Linfield, D. Ritchie, and G. Davies, *Appl. Phys. Lett.* **82**, 3165 (2003).  
<sup>6</sup>S. Kumar, Q. Hu, and J. L. Reno, *Appl. Phys. Lett.* **94**, 131105 (2009).  
<sup>7</sup>G. Scalari, M. I. Amanti, M. Fischer, R. Terazzi, C. Walther, M. Beck, and J. Faist, *Appl. Phys. Lett.* **94**, 041114 (2009).  
<sup>8</sup>M. I. Amanti, G. Scalari, R. Terazzi, M. Fischer, M. Beck, J. Faist, A. Rudra, P. Gallo, and E. Kapon, *New J. Phys.* **11**, 125022 (2009).  
<sup>9</sup>L. Sirigu, A. Rudra, E. Kapon, M. I. Amanti, G. Scalari, and J. Faist, *Appl. Phys. Lett.* **92**, 181111 (2008).  
<sup>10</sup>A. Bartels, T. Dekorsy, and H. Kurz, *Opt. Lett.* **24**, 996 (1999).  
<sup>11</sup>A. Bartels, R. Cerna, C. Kistner, A. Thoma, F. Hudert, C. Janke, and T. Dekorsy, *Rev. Sci. Instrum.* **78**, 035107 (2007).  
<sup>12</sup>R. Gebbs, G. Klatt, C. Janke, T. Dekorsy, and A. Bartels, *Opt. Express* **18**, 5974 (2010).  
<sup>13</sup>A. Bartels, T. Dekorsy, H. Kurz, and K. Köhler, *Phys. Rev. Lett.* **82**, 1044 (1999).  
<sup>14</sup>B. Jusserand and M. Cardona, "Light scattering in solids V," in *Topics in Applied Physics*, edited by M. Cardona and G. Güntherodt (Springer-Verlag, Berlin, 1989), pp. 49–152.  
<sup>15</sup>S. M. Rytov, *Akust. Zh.* **2**, 71 (1956).

- <sup>16</sup>T. Mishina, Y. Iwazaki, Y. Masumoto, and M. Nakayama, *Solid State Commun.* **107**, 281 (1998).  
<sup>17</sup>M. F. P. Winter, A. Fainstein, B. Jusserand, B. Perrin, and A. Lemaître, *Appl. Phys. Lett.* **94**, 103103 (2009).  
<sup>18</sup>S. Adachi, *J. Appl. Phys.* **58**, R1 (1985).  
<sup>19</sup>The "bulk-like" mode refers to the mode with an effective wavevector  $q = 2k_L$  to which the light would couple in absence of the folding of the acoustic phonon dispersion, i.e., if the sample would be replaced by an effective material with the same average speed of sound as the superlattice (see Ref. 14 for details).  
<sup>20</sup>W. H. Press, S. A. Teukolsky, W. T. Vetterling, and B. P. Flannery, *Numerical Recipes in C: the Art of Scientific Computing*, 2nd ed. (Cambridge University Press, Cambridge, 1992), p. 554.  
<sup>21</sup>S. Birner, T. Zibold, T. Andlauer, T. Kubis, M. Sabathil, A. Trellakis, and P. Vogl, *IEEE Trans. Electron Devices* **54**, 2137 (2007).  
<sup>22</sup>Y. Varshni, *Physica* **34**, 149 (1967).  
<sup>23</sup>M. F. Pascual Winter, G. Rozas, A. Fainstein, B. Jusserand, B. Perrin, A. Huynh, P. O. Vaccaro, and S. Saravanan, *Phys. Rev. Lett.* **98**, 265501 (2007).  
<sup>24</sup>O. Matsuda, T. Tachizaki, T. Fukui, J. J. Baumberg, and O. B. Wright, *Phys. Rev. B* **71**, 115330 (2005).  
<sup>25</sup>R. Beardsley, A. V. Akimov, B. A. Glavin, W. Maryam, M. Henini, and A. J. Kent, *Phys. Rev. B* **82**, 041302(R) (2010).  
<sup>26</sup>A complete analysis of the time evolution of spectral amplitude with time and probe wavelength is a very complex issue and is mainly determined by the opto-acoustic coupling to the quantum confined electronic states.<sup>17,23–25</sup> This point is still not well understood for much simpler systems, and is out of the scope of the present work. We intend here to give qualitative and general description.  
<sup>27</sup>The emitting performance and structure of these two THz-QCL samples have been reported in Ref. 8 as samples 3057B and 3057A, respectively.  
<sup>28</sup>N. D. Lanzillotti-Kimura, A. Fainstein, A. Huynh, B. Perrin, B. Jusserand, A. Miard, and A. Lemaître, *Phys. Rev. Lett.* **99**, 217405 (2007).  
<sup>29</sup>R. Merlin, *Solid State Commun.* **102**, 207 (1997).  
<sup>30</sup>D. Levi, S.-L. Zhang, M. V. Klein, J. Klem, and H. Morkoç, *Phys. Rev. B* **36**, 8032 (1987).  
<sup>31</sup>T. Unuma, M. Yoshita, T. Noda, H. Sakaki, and H. Akiyama, *J. Appl. Phys.* **93**, 1586 (2003).  
<sup>32</sup>N. D. Lanzillotti-Kimura, A. Fainstein, C. A. Balseiro, and B. Jusserand, *Phys. Rev. B* **75**, 024301 (2007).  
<sup>33</sup>N. D. Lanzillotti-Kimura, A. Fainstein, B. Jusserand, A. Lemaître, O. Mauguin, and L. Largeau, *Phys. Rev. B* **76**, 174301 (2007).